

# Galaxy formation in the *Planck* cosmology - I. Supplementary Material

Bruno M. B. Henriques<sup>1</sup>, Simon D. M. White<sup>1</sup>, Peter A. Thomas<sup>2</sup>,  
Raul Angulo<sup>3</sup>, Qi Guo<sup>4</sup>, Gerard Lemson<sup>1</sup>, Volker Springel<sup>5,6</sup>, Roderik Overzier<sup>7</sup>

<sup>1</sup>*Max-Planck-Institut für Astrophysik, Karl-Schwarzschild-Str. 1, D-85741 Garching b. München, Germany*

<sup>2</sup>*Astronomy Centre, University of Sussex, Falmer, Brighton BN1 9QH, UK*

<sup>3</sup>*Centro de Estudios de Física del Cosmos de Aragón, Plaza San Juan 1, Planta-2, 44001, Teruel, Spain*

<sup>4</sup>*Partner Group of the Max-Planck-Institut für Astrophysik, National Astronomical Observatories, Chinese Academy of Sciences, Beijing, 100012, China*

<sup>5</sup>*Heidelberger Institut für Theoretische Studien, Schloss-Wolfsbrunnengweg 35, D-69118 Heidelberg, Germany*

<sup>6</sup>*Zentrum für Astronomie der Universität Heidelberg, ARI, Mönchhofstr. 12-14, D-69120 Heidelberg, Germany*

<sup>7</sup>*Observatório Nacional/MCTI, Rua José Cristino, 77. CEP 20921-400, São Cristóvão, Rio de Janeiro-RJ, Brazil*

## ABSTRACT

In this supplementary material we give a full description of the treatment of astrophysical processes in our 2014 model of galaxy formation. This model is built on subhalo merger trees constructed from the Millennium and Millennium-II simulations after scaling to represent the first-year *Planck* cosmology. A set of coupled differential equations allow us to follow the evolution of six baryonic components. Five of these are associated with individual galaxies – a hot gas atmosphere, cold interstellar gas, a reservoir of gas ejected in winds, stars split into bulge, disc and intracluster light components, and central supermassive black holes. The sixth, diffuse primordial gas, is associated with dark matter which is not yet part of any halo. Primordial gas falls with the dark matter onto sufficiently massive haloes, where it is shock-heated. The efficiency of radiative cooling then determines whether it is added directly to the cold gas of the central galaxy, or resides for a while in a hot gas atmosphere. Cold interstellar gas forms stars both quiescently and in merger-induced starbursts which also drive the growth of central supermassive black holes. Stellar evolution not only determines the photometric appearance of the final galaxy, but also heats and enriches its gas components, in many cases driving material into the wind reservoir, from which it may later fall back into the galaxy. Accretion of hot gas onto central black holes gives rise to radio mode feedback, regulating condensation of hot gas onto the galaxy. Environmental processes like tidal and ram-pressure stripping and merging affect the gas components of galaxies, as well as the partition of stars between discs, bulges and the intracluster light, a diffuse component built from tidally disrupted systems. Disc and bulge sizes are estimated from simple energy and angular momentum-based arguments.

**Key words:** galaxies: formation – galaxies: evolution – galaxies: high-redshift – methods: analytical – methods: statistical

## S1 INTRODUCTION

The “Munich” model of galaxy formation is a semi-analytic scheme for simulating the evolution of the galaxy population as a whole and has been continually developed over the last quarter century (White 1989; White & Frenk 1991; Kauffmann et al. 1993, 1999; Springel et al. 2001, 2005). The 2005 completion of the Millennium Simulation enabled implementation of the model on dark matter simulations of high enough resolution to detect the structures associated with the formation of individual galaxies throughout cosmologi-

cally relevant volumes. Updates to the baryonic physics have resulted in a series of publicly released galaxy/halo/subhalo catalogues that have been widely used by the community (Croton et al. 2006; De Lucia & Blaizot 2007; Bertone et al. 2007; Guo et al. 2011, 2013).<sup>1</sup> The model of the current paper updates that of Guo et al. (2011), aiming at better representation of the observed build-up over time and of the present star formation activity of the low-mass galaxy

<sup>1</sup> See <http://www.mpa-garching.mpg.de/millennium>

population ( $8.0 \leq \log M_*/M_\odot \leq 9.5$ ). Guo et al. (2011) itself updated earlier treatments of supernova feedback and of galaxy mergers in order to agree better with observations of dwarf and satellite galaxies. It also introduced detailed tracking of the angular momentum of different galaxy components so that the size evolution of discs and bulges could be followed. Finally, Guo et al. (2013) implemented the procedure of Angulo & White (2010) so that the Millennium Simulation could be used to model evolution in cosmologies other than its native *WMAP1* cosmology.

In this Supplementary Material we aim to give a detailed and fully self-contained summary of the treatment of baryonic physics in our current model. Many aspects of this are unchanged since earlier models but repetition of material in a single coherent and complete description seems preferable to referring each model element back to the particular earlier paper where it was first used. We anticipate updating this supplementary material as future versions of our model are released, so that each will have its own full astrophysics and algorithmic summary.

### S1.1 Dark Matter Simulations

The galaxy formation model of this paper is built on subhalo merger trees describing the evolution of dark matter structures in two large dark matter simulations, the Millennium (Springel et al. 2005) and Millennium-II (Boylan-Kolchin et al. 2009) simulations. Both assume a  $\Lambda$ CDM cosmology with parameters derived by a combined analysis of the 2dFGRS (Colless et al. 2001) and the first-year *WMAP* data (Spergel et al. 2003):  $\sigma_8 = 0.9$ ,  $H_0 = 73 \text{ km s}^{-1} \text{ Mpc}^{-1}$ ,  $\Omega_\Lambda = 0.75$ ,  $\Omega_m = 0.25$ ,  $\Omega_b = 0.045$  and  $n = 1.0$ . For this work the original cosmology has been scaled, using the Angulo & White (2010) technique, as updated by Angulo & Hilbert (2015), to represent the best-fitting cosmological parameters derived from the first-year *Planck* data. The underlying cosmology of the dark matter simulations and thus the galaxy formation model is then:  $\sigma_8 = 0.829$ ,  $H_0 = 67.3 \text{ km s}^{-1} \text{ Mpc}^{-1}$ ,  $\Omega_\Lambda = 0.685$ ,  $\Omega_m = 0.315$ ,  $\Omega_b = 0.0487$  ( $f_b = 0.155$ ) and  $n = 0.96$ .

Both the Millennium and Millennium-II simulations trace  $2160^3$  ( $\sim 10$  billion) particles from  $z = 127$  to the present day. The Millennium was carried out in a box of original side  $500 h^{-1} \text{ Mpc} = 685 \text{ Mpc}$ . After rescaling to the *Planck* cosmology, the box size becomes  $714 \text{ Mpc}$ , implying a particle mass of  $1.43 \times 10^9 M_\odot$ . The Millennium-II follows a region a fifth the linear size, resulting in 125 times better mass resolution. Combined, the two simulations follow dark matter haloes which host galaxies spanning five orders of magnitude in stellar mass at  $z = 0$ . The particle data were stored in 64 and 68 output snapshots, respectively, for the Millennium and Millennium-II with the last 60 overlapping between the two simulations. After rescaling, the last five snapshots of each simulation correspond to the future, and  $z = 0$  corresponds to the sixth from last of the original snapshots. At each time the data were post-processed in order to produce a friend-of-friends (FOF) group catalogue by joining particles separated by less than 20% of the mean interparticle spacing (Davis et al. 1985). The SUBFIND algorithm (Springel et al. 2001) was then applied to identify all the self-bound substructures in each FOF group. The radius of the FOF group is defined as the radius of the largest

sphere centered on the potential minimum which contains an overdensity larger than 200 times the critical value. The group mass is then the total mass within this sphere and other group properties are related by:

$$M_{200c} = \frac{100}{G} H^2(z) R_{200c}^3 = \frac{V_{200c}^3}{10 GH(z)}, \quad (\text{S1})$$

where  $H(z)$  is the Hubble constant at redshift  $z$ .

Every subhalo in a given snapshot which contains 20 or more bound particles is connected to a unique descendant in the subsequent snapshot and these links are then used to build subhalo merger trees which encode the assembly history of every subhalo identified at  $z = 0$ . These trees are the basis on which the galaxy formation model is constructed (see Springel et al. 2005). They allow us to build much more realistic satellite galaxy populations than would be possible using trees linking the FOF haloes themselves. The most massive subhalo in each FOF group is usually much bigger than all the others, and is defined as the “main halo”: the group central galaxy (which we often refer to as a “type 0” galaxy) is located at the minimum of the potential of this main halo. All other bound subhaloes contain satellite galaxies at their centres (type 1’s). In addition, our galaxy formation model follows satellites which have already lost their own dark matter subhaloes but which are yet to merge with the central galaxy. Such objects are referred to as “type 2” galaxies or “orphan” satellites. Their position and velocity are tied to those of the dark matter particle that was the most bound within their subhalo at the last time that this was identified by SUBFIND with at least 20 particles.

### S1.2 Overview of the galaxy formation physics

Our model for galaxy formation starts by assigning a cosmic abundance of baryons to each collapsed dark matter halo. Subsequent growth brings its fair share of baryons in the form of primordial diffuse gas which shock-heats and then either cools immediately onto the disc of the central galaxy, or is added to a quasi-static hot atmosphere which accretes more slowly through a cooling flow. The disc of cold gas fuels the formation of stars which eventually die, releasing energy, mass and heavy elements into the surrounding medium. This energy reheats cold disc gas, injecting it into a hot atmosphere, which may itself also be ejected into an external reservoir to be reincorporated only at some much later time. Black holes are assumed to grow primarily through the accretion of cold gas during mergers, but also through quiescent accretion from the hot atmosphere, which releases energy which can counteract the cooling flow. This form of feedback eventually curtails star formation in the most massive systems. A number of environmental processes act on satellites as soon as they cross the virial radius of their host. Tidal forces are assumed to remove hot gas, cold gas and stars while hot gas is also removed by ram-pressure stripping. These processes gradually quench star formation, particularly in satellites orbiting within more massive systems. As dark matter subhaloes merge, so do their associated galaxies, although with some delay. Once a subhalo is fully disrupted, its galaxy spirals into the central galaxy, merging after a dynamical friction time and creating a bulge and a burst of star formation. Bulges also form through secular processes whenever discs become sufficiently massive

to be dynamically unstable. Finally, the light emitted from stellar populations of different ages is computed via population synthesis models and dust extinction corrections are applied. The uncertain efficiencies and scalings characterising all these physical processes are simultaneously determined by using MCMC techniques to fit a set of calibration observations (in this paper, abundances and passive fractions as a function of stellar mass at a variety of redshifts).

### S1.3 Infall and reionization

Following the standard White & Frenk (1991) approach we assume that each collapsed dark matter structure will, at every time, have a mass of associated baryons given by the cosmic mean baryon fraction,  $f_b^{\text{cos}} = 15.5\%$  for the *Planck* cosmology. As haloes grow, we assume that matter that was not previously part of any object is added in these same proportions, with the baryons in the form of diffuse primordial gas which shock-heats on accretion, thereafter either cooling again immediately or being added to a quasi-static hot atmosphere.

For sufficiently low-mass haloes and over a large part of cosmic history this simple picture needs modification, since photo-heating by the UV background field raises the temperature of diffuse intergalactic gas to the point where pressure effects prevent it from accreting onto haloes with the dark matter (Efstathiou 1992). In order to model this, we use results from Gnedin (2000) who defines a filtering halo mass,  $M_F(z)$ , below which the baryonic fraction is reduced with respect to the universal value according to:

$$f_b(z, M_{200c}) = f_b^{\text{cos}} \left( 1 + (2^{\alpha/3} - 1) \left[ \frac{M_{200c}}{M_F(z)} \right]^{-\alpha} \right)^{-3/\alpha}. \quad (\text{S2})$$

For haloes with  $M_{200c} > M_F$  suppression of the baryon fraction is small, but for haloes with  $M_{200c} \ll M_F(z)$  the baryon fraction drops to  $(M_{200c}/M_F(z))^3$ . We adopt  $\alpha = 2$  and take  $M_F(z)$  from the numerical results of Okamoto et al. (2008).  $M_F$  varies from  $\sim 6.5 \times 10^9 M_\odot$  at  $z = 0$ , to  $\sim 10^7 M_\odot$  just before reionization starts at  $z = 8$ .

### S1.4 Cooling modes

Infalling diffuse gas is expected to shock-heat as it joins a halo. At early times and for low-mass haloes the accretion shock happens close to the central object and the post-shock cooling time is short enough that new material settles onto the cold gas disc at essentially the free-fall rate. At later times and for higher mass haloes the accretion shock moves away from the central object, settling at approximately the virial radius, while the post-shock cooling time exceeds the halo sound crossing time. The shocked heated gas then forms a quasi-static hot atmosphere from which it can gradually accrete to the centre via a cooling flow. The halo mass separating these two regimes is  $\sim 10^{12} M_\odot$  (White & Rees 1978; White & Frenk 1991; Forcada-Miro & White 1997; Birnboim & Dekel 2003). In a realistic, fully three-dimensional situation a hot quasi-static atmosphere can coexist with cold inflowing gas streams in haloes near the transition mass (Kereš et al. 2005; Nelson et al. 2013) but the overall rate of accretion onto the central object remains similar to that given

by the formulae below (Benson et al. 2001; Yoshida et al. 2002).

Following the formulation of White & Frenk (1991) and Springel et al. (2001), we assume that, in the quasi-static regime, gas cools from a hot atmosphere where its distribution is isothermal. The cooling time is then given by the ratio between the thermal energy of the gas and its cooling rate per unit volume:

$$t_{\text{cool}}(r) = \frac{3\mu m_{\text{H}} k T_{200c}}{2\rho_{\text{hot}}(r)\Lambda(T_{\text{hot}}, Z_{\text{hot}})}, \quad (\text{S3})$$

where  $\mu m_{\text{H}}$  is the mean particle mass,  $k$  is the Boltzmann constant,  $\rho_{\text{hot}}(r)$  is the hot gas density and  $Z_{\text{hot}}$  is the hot gas metallicity.  $T_{\text{hot}}$  is the temperature of the hot gas which is assumed to be the virial temperature of the halo given by  $T_{200c} = 35.9 (V_{200c}/\text{km s}^{-1})^2 \text{K}$  (for subhaloes we use this temperature as estimated at infall).  $\Lambda(T_{\text{hot}}, Z_{\text{hot}})$  is the equilibrium cooling function for collisional processes which depends both on the metallicity and temperature of the gas but ignores radiative ionization effects (Sutherland & Dopita 1993). The hot gas density as a function of radius for a simple isothermal model is given by:

$$\rho_{\text{hot}}(r) = \frac{M_{\text{hot}}}{4\pi R_{200c} r^2} \quad (\text{S4})$$

and assuming that the cooling radius is where the cooling time equals the halo dynamical time:

$$r_{\text{cool}} = \left[ \frac{t_{\text{dyn,h}} M_{\text{hot}} \Lambda(T_{\text{hot}}, Z_{\text{hot}})}{6\pi \mu m_{\text{H}} k T_{200c} R_{200c}} \right]^{\frac{1}{2}}, \quad (\text{S5})$$

where  $t_{\text{dyn,h}}$  is the halo dynamical time defined as  $R_{200c}/V_{200c} = 0.1H(z)^{-1}$  (De Lucia et al. 2004). The specific choice of coefficient for the dynamical time of the halo is, of course, somewhat arbitrary.

When  $r_{\text{cool}} < R_{200c}$  we assume that the halo is in the cooling flow regime with gas cooling from the quasi-static hot atmosphere at a rate:

$$\dot{M}_{\text{cool}} = M_{\text{hot}} \frac{r_{\text{cool}}}{R_{200c}} \frac{1}{t_{\text{dyn,h}}}. \quad (\text{S6})$$

When  $r_{\text{cool}} > R_{200c}$  the halo is in the rapid infall regime and material accretes onto the central object in free fall, thus on the halo dynamical time:

$$\dot{M}_{\text{cool}} = \frac{M_{\text{hot}}}{t_{\text{dyn,h}}}. \quad (\text{S7})$$

This particular formula for rapid infall was introduced in Guo et al. (2011) in order to ensure a smooth transition between the two regimes.

### S1.5 Disc formation and angular momentum

As primordial material accretes onto a halo, its dark matter and baryonic components are expected to have similar specific angular momenta. Some of this gas is subsequently added to the central galaxy, and its remaining angular momentum then determines the radius at which it settles within the galactic disc. We follow these processes using the simple model introduced by Guo et al. (2011). The properties of the cold gas and stellar discs are calculated separately and their time evolution is modelled explicitly. The angular

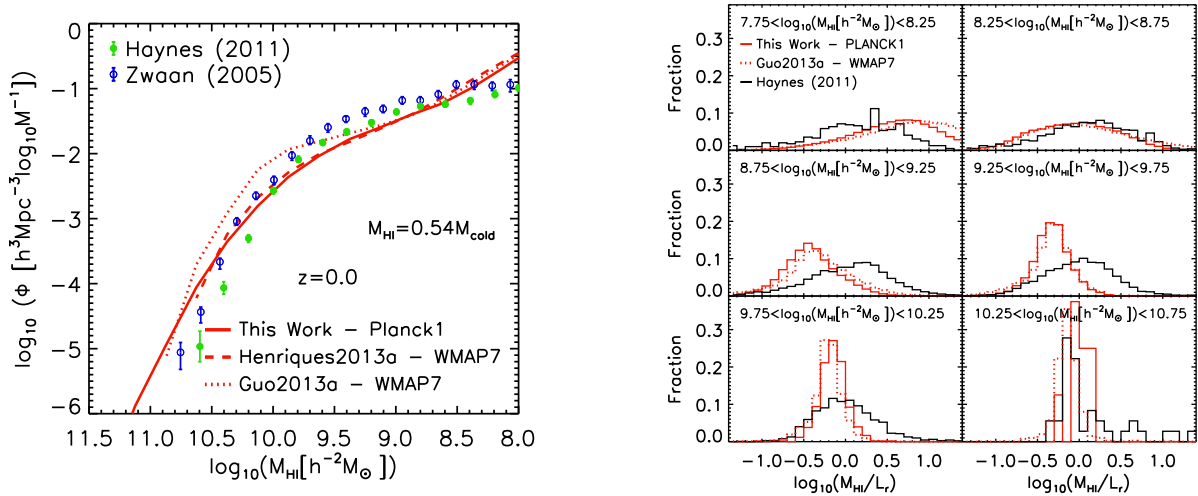


**Figure S1.** Left: The mass function of atomic gas at  $z = 0$ , defined as  $0.54 \times M_{\text{cold}}$ . Observational data from Zwaan et al. (2005) and Haynes et al. (2011) are compared with the current version of the model (solid red line) and with the models of Henriques et al. (2013) (dashed red line) and Guo et al. (2013) (dotted red line). Right: Histograms of the ratio of cold gas mass to  $r$ -band luminosity in different bins of atomic gas mass. The current model (solid red line) and that of Guo et al. (2013) (dotted red lines) are compared with the HI-flux-limited sample of Haynes et al. (2011) from ALFALFA (solid black line).

momentum of the cold gas disc changes as a result of star formation and of gas accretion through cooling and minor merger events:

$$\Delta \vec{J}_{\text{gas}} = \delta \vec{J}_{\text{gas,cooling}} + \delta \vec{J}_{\text{gas,SF}} + \delta \vec{J}_{\text{gas,acc.}} \quad (\text{S8})$$

The various terms in this expression can be written out explicitly as:

$$\begin{aligned} \Delta \vec{J}_{\text{gas}} &= \frac{\vec{J}_{\text{DM}}}{M_{\text{DM}}} \dot{M}_{\text{cool}} \delta t - \frac{\vec{J}_{\text{gas}}}{M_{\text{gas}}} ((1 - R_{\text{ret}}) \dot{M}_{\star} \delta t + \Delta M_{\text{reheat}}) \\ &+ \frac{\vec{J}_{\text{DM}}}{M_{\text{DM}}} M_{\text{sat,gas}}, \end{aligned} \quad (\text{S9})$$

where  $\delta t$  is the time interval considered,  $\dot{M}_{\text{cool}}$  is the cooling rate (from Eq. S6 or S7),  $(1 - R_{\text{ret}}) \dot{M}_{\star}$  is the formation rate of long lived stars (from eq. S14 below),  $\Delta M_{\text{reheat}}$  is the cold gas reheated into the hot atmosphere as a result of star formation activity (see eq. S18 and following text below), and  $M_{\text{sat,gas}}$  is the cold gas mass of any merging satellite(s). Gas coming from cooling events or minor mergers is thus assumed to have the mean specific angular momentum of the dark matter halo ( $\vec{J}_{\text{DM}}/M_{\text{DM}}$ ), while star formation and reheating are assumed to affect gas with the mean specific angular momentum of the cold gas disc ( $\vec{J}_{\text{gas}}/M_{\text{gas}}$ ). The stellar disc gains the angular momentum which is removed from the gas disc by star formation events,  $\delta \vec{J}_{\star} = (\vec{J}_{\text{gas}}/M_{\text{gas}})(1 - R_{\text{ret}}) \dot{M}_{\star} \delta t$ , and in our model, this is the only process that changes the angular momentum of the stellar disc; stars accreted in minor mergers are added to the bulge and secular instabilities are assumed to transfer negligible angular momentum from disc to bulge.

To compute sizes for the stellar and gaseous discs we assume them to have exponential surface density profiles and flat rotation curves. The corresponding scale-lengths can then be calculated as:

$$R_{\text{gas}} = \frac{J_{\text{gas}}/M_{\text{gas}}}{2V_{\text{max}}} \quad (\text{S10})$$

and

$$R_{\star} = \frac{J_{\star}/M_{\star,d}}{2V_{\text{max}}}, \quad (\text{S11})$$

where  $M_{\text{gas}}$  and  $M_{\star,d}$  are the total masses of the gas and stellar discs, respectively, and the rotation velocity of both discs is approximated by the maximum circular velocity of their host halo,  $V_{\text{max}}$ . This simple picture needs modification if baryons have a significant impact on the inner structure of their dark matter haloes. We refer the reader to Guo et al. (2011) for further discussion and for a comparison between predicted and observed disc sizes.

With these assumptions, the surface density profiles of the gas and stellar discs are given by:

$$\Sigma_{\text{gas}}(R) = \Sigma_{\text{gas},0} \exp(-R/R_{\text{gas}}) \quad (\text{S12})$$

and

$$\Sigma_{\star}(R) = \Sigma_{\star,0} \exp(-R/R_{\star}), \quad (\text{S13})$$

where  $\Sigma_{\text{gas},0} = M_{\text{gas}}/2\pi R_{\text{gas}}^2$  and  $\Sigma_{\star,0} = M_{\star}/2\pi R_{\star}^2$  are the central surface densities of the cold gas and stellar discs.

## S1.6 Star formation

As noted in the last section, stars are assumed to form from cold gas within the disc of each galaxy. The star formation rate is taken to be:

$$\dot{M}_{\star} = \alpha_{\text{SF}} \frac{(M_{\text{gas}} - M_{\text{crit}})}{t_{\text{dyn,disk}}}, \quad (\text{S14})$$

where  $M_{\text{gas}}$  is again the total mass of cold gas,  $t_{\text{dyn,disk}} = R_{\star}/V_{\text{max}}$ , is the dynamical time of the disc, and  $M_{\text{crit}}$  is a threshold mass (see below). From the total mass of stars formed,  $\dot{M}_{\star}$ , we assume that a fraction  $R_{\text{ret}}$  is associated with massive, short-lived, stars and is immediately returned to the cold gas.  $R_{\text{ret}} = 0.43$  is determined from the Chabrier (2003) initial mass function. Thus the stellar mass of the

disc is augmented by  $\delta M_\star = (1 - R_{\text{ret}})\dot{M}_\star \delta t$  and the cold disc mass is reduced by the same amount.

Applying the arguments of Kauffmann (1996) we set the threshold mass for star formation,  $M_{\text{crit}}$ , to be:

$$M_{\text{crit}} = M_{\text{crit},0} \left( \frac{V_{200c}}{200 \text{ km s}^{-1}} \right) \left( \frac{R_{\text{gas}}}{10 \text{ kpc}} \right). \quad (\text{S15})$$

Since Kauffmann et al. (1999) all versions of the Munich model have adopted  $M_{\text{crit},0} = 3.8 \times 10^9 M_\odot$  which still appears tenable in comparison with some recent observations in the Milky Way (Lada et al. 2010; Heiderman et al. 2010). However, this and other work (Bigiel et al. 2008; Leroy et al. 2008) suggest that star formation should be linked explicitly to a molecular gas component rather than to the total amount of cold gas. Recently, Fu et al. (2012, 2013) introduced a detailed prescription for the evolution of atomic and molecular components into the Munich semi-analytic model, allowing star formation to be connected directly to molecular content (similar developments were included in the Durham model by Lagos et al. 2011). This is clearly more realistic than eq. (S15) and will be incorporated in future large-scale modelling efforts, but here we simply allow the star formation threshold  $M_{\text{crit},0}$  to be a free parameter in our MCMC sampling, recognising that our previous fixed value was poorly justified. The new preferred value is about a factor of two smaller, mainly in order to slow the quenching of satellites by allowing them to use up a larger fraction of the cold gas with which they fall into their host.

Fig. S1 compares our new model’s predictions for the atomic gas mass function (left panel) and for the atomic gas over luminosity ratios (right panel) in HI mass-limited bins. The reduced threshold still results in reasonable gas properties but there is a significant deficit of cold gas around the knee of the mass function for atomic gas. In this respect, the earlier model of Guo et al. (2013) does significantly better than the current model, presumably because of its higher star formation threshold and lower star formation efficiency. We note that, since our model does not distinguish between different cold gas phases, an ideal comparison would be with observations of the total cold gas in discs. This would avoid an arbitrary choice for the atomic fraction in the model. However, despite considerable progress in recent years, there are still no large, representative samples providing the HI+H<sub>2</sub> content of galaxies. Available H<sub>2</sub> samples are limited in terms of both size and selection. The results of these surveys are nevertheless useful, in that they show that the scatter in molecular to atomic ratio is smaller than could be inferred from earlier work (Saintonge et al. 2011, Bothwell et al. 2014), that the typical molecular/total gas fraction is about 25%, dropping to smaller mean values at lower stellar mass, and that few galaxies have a value exceeding 50%. This shows the factor of 0.54 which we use to convert total gas mass to HI mass in Fig.1 (a factor of 0.75 to account for helium and a factor of 0.7 to account for H<sub>2</sub>) is quite reasonable, and that the scatter in molecular-to-atomic ratio is too small to affect the predicted distributions very strongly, given their width.

Stars can also form whenever two galaxies merge since their cold gas components are strongly disturbed, typically initiating a starburst and feeding some cold gas into the central black hole. This and all other merger-related processes are described in Section S1.12.

## S1.7 Supernova feedback

Massive stars are relatively short-lived. Consequently, soon after an episode of star formation, a large number of them explode as supernovae, strongly clustered both in space and time. The collective energy released by these supernovae and by the stellar winds which precede them is injected into surrounding gas, both cold and hot. As a result, some of the cold interstellar medium is reheated to join the hot gas atmosphere, and this atmosphere itself is also heated, compensating for its cooling and causing some of it to flow out of the galaxy in a wind. This feedback process is a critical aspect of galaxy formation and has long been identified as the main agent controlling its overall efficiency (Larson 1974; White & Rees 1978; Dekel & Silk 1986). As a result, detailed modelling is required if a simulation is to produce a realistic galaxy population. Our specific feedback model is controlled by two main efficiencies, each with three adjustable parameters. One efficiency sets the fraction of the “SN” energy which is available to drive long-term changes in the thermodynamic state of the galaxy’s gas components (rather than being lost to cooling radiation), while the other controls the fraction of this energy which is used to reheat cold gas and inject it into the hot gas atmosphere, the remainder being used to heat this atmosphere directly. Heating of the hot atmosphere results in ejection of “wind” material to an external reservoir from which it may or may not be reincorporated at a later time, depending on the mass of the host system.

The energy effectively available to the gas components from supernovae and stellar winds is taken to be:

$$\Delta E_{\text{SN}} = \epsilon_{\text{halo}} \times \frac{1}{2} \Delta M_\star V_{\text{SN}}^2, \quad (\text{S16})$$

where  $\frac{1}{2} V_{\text{SN}}^2$  is the mean energy injected per unit mass of stars formed (we take  $V_{\text{SN}} = 630 \text{ km s}^{-1}$ ) and the efficiency is

$$\epsilon_{\text{halo}} = \eta \times \left[ 0.5 + \left( \frac{V_{\text{max}}}{V_{\text{eject}}} \right)^{-\beta_2} \right]. \quad (\text{S17})$$

The mass of cold gas reheated by star formation and added to the hot atmosphere is assumed to be directly proportional to the amount of stars formed:

$$\Delta M_{\text{reheat}} = \epsilon_{\text{disk}} \Delta M_\star, \quad (\text{S18})$$

where the second efficiency is

$$\epsilon_{\text{disk}} = \epsilon \times \left[ 0.5 + \left( \frac{V_{\text{max}}}{V_{\text{reheat}}} \right)^{-\beta_1} \right]. \quad (\text{S19})$$

This reheating is assumed to require energy  $\Delta E_{\text{reheat}} = \frac{1}{2} \Delta M_{\text{reheat}} V_{200c}^2$ . If  $\Delta E_{\text{reheat}} > \Delta E_{\text{SN}}$ , the reheated mass is assumed to saturate at  $\Delta M_{\text{reheat}} = \Delta E_{\text{SN}} / (\frac{1}{2} V_{200c}^2)$ . Otherwise, the remaining SN energy is used to eject a mass  $\Delta M_{\text{eject}}$  of hot gas into an external reservoir, where

$$\frac{1}{2} \Delta M_{\text{eject}} V_{200c}^2 = \Delta E_{\text{SN}} - \Delta E_{\text{reheat}}. \quad (\text{S20})$$

There is now considerable observational evidence for ejection of interstellar gas due to star formation activity (Shapley et al. 2003; Rupke et al. 2005; Weiner et al. 2009; Martin et al. 2012; Rubin et al. 2013). While the overall impact of such processes is still debated, observations of rapidly

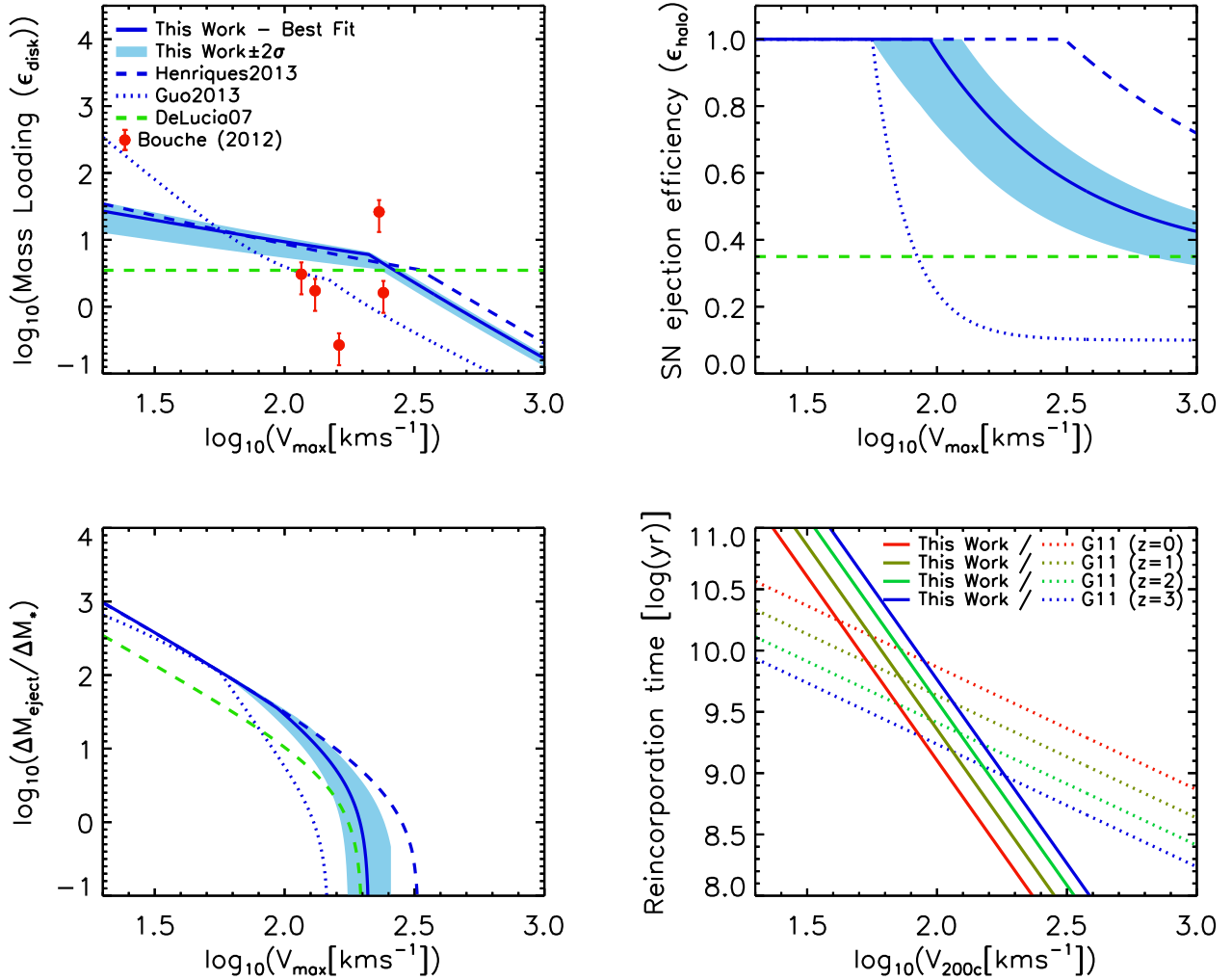


**Figure S2.** Illustration of the dependences of SN feedback on halo properties. The top left panel shows the disc reheating efficiency  $\epsilon_{\text{disk}}$  as a function of maximum circular velocity  $V_{\text{max}}$ . Often referred to as the mass-loading factor, this is the ratio of the star formation rate to the rate at which ISM material is heated and injected into the hot halo. The top right panel shows the halo ejection efficiency  $\epsilon_{\text{halo}}$  as a function of  $V_{\text{max}}$ . This is the fraction of the available SN energy which is used in reheating disc gas and in ejecting hot gas from the halo. The bottom left panel gives  $\Delta M_{\text{eject}}/\Delta M_{\star}$ , the ratio between the hot gas mass ejected to an external reservoir and the cold gas mass which is turned into stars. The bottom right panel shows the reincorporation time-scale  $t_{\text{reinc}}$  as a function of halo virial velocity  $V_{200c}$  and of redshift (note that the redshift evolution comes solely from the evolution in the relation between  $V_{200c}$  and  $M_{200c}$ ). In each panel dashed green lines refer to the De Lucia & Blaizot (2007) model, dotted blue lines to the G11-WMAP7 model, dashed blue lines to the Henriques et al. (2013) model and solid blue lines to our new model with its best-fitting parameter values. The blue shaded regions give the  $2\sigma$  range allowed by our MCMC sampling. Colours in the bottom right panel indicate redshift as shown by the label.

star-forming systems tend to favour mass-loading factors (the ratio of reheated mass to the mass of stars formed) between 1 and 10. The mass-loading factors preferred by our MCMC chains are shown as a function of virial velocity in the top left panel of Fig. S2 and seem similar or somewhat larger than observed.

Ejection of disc gas into the hot atmosphere has relatively little impact when the latter has a short cooling time, since this effectively drives a galactic fountain in which the material soon returns and becomes available for star formation again. Ejection of gas from the hot phase to an external reservoir has substantially stronger long-term effects, however, since such wind ejecta are unavailable for star forma-

tion for much longer periods. The top right panel of Fig. S2 shows  $\epsilon_{\text{halo}}$ , the fraction of the available energy that is used in feedback processes, as a function of virial velocity, while the bottom left panel shows  $\Delta M_{\text{eject}}/\Delta M_{\star}$ , the ratio of the mass of gas ejected in a wind from the galaxy/halo system to the mass of stars formed. For the parameters preferred by our MCMC chains, the available energy is used with high efficiency in low-mass systems, and winds are able to eject material from the haloes of all galaxies with virial velocity less than about  $200 \text{ km s}^{-1}$ .

### S1.7.1 SN feedback in satellite galaxies <sup>2</sup>

The details of gas reheating and ejection just described, accurately represent the impact of SN feedback in isolated galaxies and in galaxies at the centre of an FoF group (type 0's). For satellites at the centre of a subhalo (type 1's), or orphan satellites with no dark matter, hot or ejected gas (type 2's), the impact of environment must be taken into account. When gas is reheated into the hot phase of a type 1 galaxy, either its own cold gas or gas originated at a type 2 satellite, a fraction is immediately removed due to tidal stripping. In type 2's, reheating will move their own cold gas into the hot phase of their direct central companion, either a type 1 galaxy at the centre of a subhalo or a type 0 galaxy at the centre of the main halo, from which the left-over energy will eject material.

When calculating the amount of energy available from SN and the reheating efficiency, eqs. S17 and S19, we always use the  $V_{\max}$  of the halo from where the gas will be moved, using the value at infall for satellites. The value for the virial temperature at which reheating saturates and the escape velocity of haloes at which gas is ejected are always taken from the halo where the gas will end up.

### S1.8 Reincorporation of gas ejected in winds

A number of recent papers have argued that most published semi-analytic models and cosmological hydrodynamics simulations form low-mass galaxies ( $8.0 \leq \log M_*/M_\odot \leq 9.5$ ) too early, leading to an overabundance of these objects at  $z \geq 1$  (Fontanot et al. 2009; Henriques et al. 2011; Guo et al. 2011; Weinmann et al. 2012; Lu et al. 2014; Genel et al. 2014; Vogelsberger et al. 2014). In the context of the Munich galaxy formation model, the MCMC analysis of Henriques et al. (2013) concluded that this can only be corrected by coupling strong winds in low-mass galaxies with long reincorporation times for the ejecta. This results in slower growth at early times followed by a stronger build-up between  $z = 2$  and 0 as the ejecta finally fall in again.

In the current work we adopt the implementation of Henriques et al. (2013). The mass of gas returned to the hot gas halo from the ejecta reservoir is taken to be:

$$\dot{M}_{\text{ejec}} = -\frac{M_{\text{ejec}}}{t_{\text{reinc}}}, \quad (\text{S21})$$

where the reincorporation time-scales inversely with the mass of the host halo,

$$t_{\text{reinc}} = \gamma' \frac{10^{10} M_\odot}{M_{200c}}, \quad (\text{S22})$$

rather than with the ratio of its dynamical time and circular velocity, as in Guo et al. (2011). Note that a key aspect of this phenomenological model is that diffuse gas is not available for cooling onto the central galaxy as long as it remains in the external reservoir. The precise location of this reservoir is unspecified, and the gas may not leave the halo entirely. Rather, its entropy may simply be raised above the level assumed by our simple ‘‘isothermal’’ model, in which case the reincorporation time-scales should be interpreted

<sup>2</sup> This section was not included in the published version of the paper, only in the arxiv re-submission.

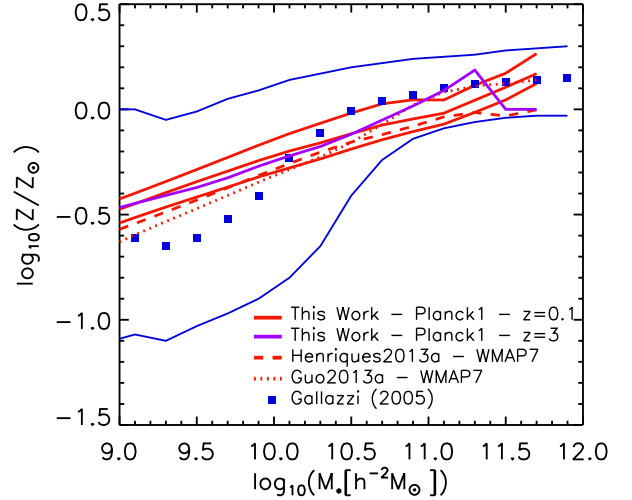


**Figure S3.** Metallicity as a function of stellar mass at  $z = 0.1$ . Observational data from Gallazzi et al. (2005) are compared to the current model (solid red line) and to the earlier models of Henriques et al. (2013) (dashed red line) and Guo et al. (2013) (dotted red line). Predictions from the current model at  $z = 3$  are plotted as a solid purple line.

as the time needed to cool to the point where the gas can again be considered part of our standard cooling flow.

The differences between the new reincorporation times and those adopted in Guo et al. (2011) are shown as a function of virial velocity and redshift in the lower right panel of Fig. S2. Note that the redshift dependence in our new model simply results from the relation between  $M_{200c}$  and  $V_{200c}$  (eq. S1). In practice gas ejected in winds from low-mass haloes will never be reincorporated unless they become part of a more massive system, while gas returns immediately in the most massive haloes. This implementation agrees qualitatively with the behaviour seen by Oppenheimer & Davé (2008) and Oppenheimer et al. (2010) in their numerical simulations.

### S1.9 Metal enrichment

When stars die, they release newly formed heavy elements into the surrounding medium in addition to mass and energy. In the current work, we follow the total mass of metals only, assuming that each solar mass of stars produces a mass  $y$  of heavy metals, with this ‘‘yield’’ treated as a free parameter in the MCMC. The newly formed metals are mixed instantaneously into the cold gas, and thereafter follow it through the various baryonic components of the galaxy, thus enriching the hot gas atmosphere and future generations of stars. In recent work, Yates et al. (2013) and De Lucia et al. (2014) have introduced two different implementations of chemical enrichment into the Munich model. These follow in detail the return of individual elements as stellar populations age, and include metallicity-dependences both in the yields and in population evolution modelling. We expect to incorporate such effects in future large-scale population models, but they are ignored in the model presented here.

The metallicities predicted by the current model are il-

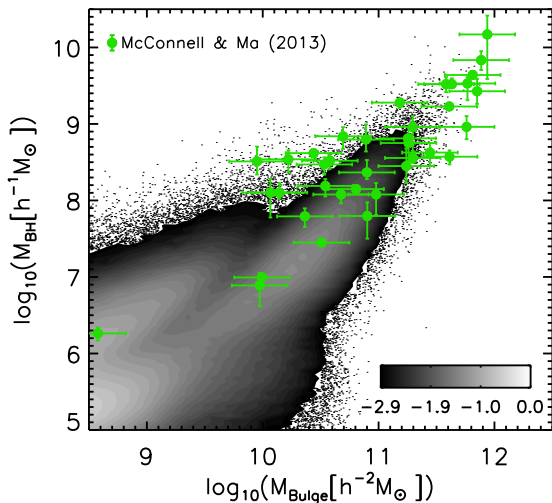


**Figure S4.** Comparison between theoretical predictions from the current model (normalized number density of galaxies shown as logarithmic grey-scale contours and dots) and observations from McConnell & Ma (2013) (green circles) for the black hole-bulge mass relation at  $z = 0$

illustrated in Fig. S3, where the theoretical stellar mass-stellar metallicity relation at  $z = 0$  is compared with observations. The current model and those of Henriques et al. (2013) and Guo et al. (2013) all show similar stellar metallicities, despite significant changes in the treatment of wind ejecta. The  $z = 3$  predictions of the current model (and also of the earlier ones) show chemical enrichment to happen very early. The same behaviour is found for the metallicity of the cold gas. This appears to disagree with observation (Maiolino et al. 2008) so further work is clearly needed on this point.

### S1.10 Black hole related processes

In our model, the energy released by supernovae and stellar winds has a dramatic effect on low-mass galaxies, but is unable to reduce cooling onto massive systems ( $\log M_*/M_\odot \geq 10.5$ ) to the very low rates inferred from their observed stellar masses and star formation rates. We follow Croton et al. (2006) in assuming that feedback from central supermassive black holes is the agent that terminates galaxy growth in massive haloes. Black holes are taken to form and to grow when cold gas is driven to the centre of merging systems. In addition, pre-existing black holes merge as soon as their host galaxies do. This “quasar mode” growth is the main channel by which black holes gain mass in our model, but we do not associate it with any feedback beyond that from the strong starbursts which accompany gas-rich mergers. Black holes are also allowed to accrete gas from the hot gas atmospheres of their galaxies, however, and this is assumed to generate jets and bubbles which produce radio mode feedback, suppressing cooling onto the galaxy and so eliminating the supply of cold gas and quenching star formation. The relative importance of these two modes to black hole growth is shown as a function of time and galaxy mass in Fig. 3 of Croton et al. (2006).

#### S1.10.1 Quasar mode - black hole growth

Whenever two galaxies merge, their cold gas components are strongly disturbed and a significant fraction is driven into the inner regions where it may form a black hole or be accreted onto a pre-existing black hole. When both galaxies contain a pre-existing black hole, these are expected to merge during this highly dynamic phase of evolution.

The amount of gas accreted in the quasar mode is taken to depend on the properties of the two merging galaxies as,

$$\Delta M_{\text{BH,Q}} = \frac{f_{\text{BH}}(M_{\text{sat}}/M_{\text{cen}}) M_{\text{cold}}}{1 + (V_{\text{BH}}/V_{200c})^2}, \quad (\text{S23})$$

where  $M_{\text{cen}}$  and  $M_{\text{sat}}$  are the total baryon masses of the central galaxy and the satellite which merges with it,  $M_{\text{cold}}$  is their total cold gas mass,  $V_{200c}$  is the virial velocity of the central halo and  $f_{\text{BH}}$  and  $V_{\text{BH}}$  are two adjustable parameters which control the fraction of the available cold gas that is accreted and the virial velocity at which the efficiency saturates. The mass of the black hole at the centre of the final merged galaxy is thus taken to be  $M_{\text{BH,f}} = M_{\text{BH,1}} + M_{\text{BH,2}} + \Delta M_{\text{BH,Q}}$  where the subscripts 1 and 2 denote the masses of the progenitor black holes.

Mass accretion during mergers is the main channel of black hole growth in our model. The fact that bulges and black holes are formed in related processes results in a tight relation between black hole and bulge masses. The same is seen in observations and is shown in Fig. S4, where we compare the predicted black hole-bulge mass relation for the new model (gray contours) with observations from McConnell & Ma (2013) (green points).

#### S1.10.2 Radio mode - feedback

We assume that central supermassive black holes continually accrete gas from the hot gas atmosphere of their host galaxies, and that this produces radio mode feedback which injects energy into the hot atmosphere. Recent changes to our model have increased the amount of hot gas available to cool onto massive systems at late times, and as a result we find that the original Croton et al. (2006) model for radio mode feedback is unable to suppress star formation sufficiently just above the knee of the galaxy stellar mass function. An MCMC analysis shows that this cannot be solved simply by changing parameters in the original formulation, but that acceptable results can be obtained by assuming the accretion rate to be given by

$$\dot{M}_{\text{BH}} = k_{\text{AGN}} \left( \frac{M_{\text{hot}}}{10^{11} M_\odot} \right) \left( \frac{M_{\text{BH}}}{10^8 M_\odot} \right). \quad (\text{S24})$$

This formula is equivalent to that of Croton et al. (2006) divided by a factor of  $H(z)$ , so accretion is enhanced at lower redshifts. The differences in the treatment of AGN growth and feedback between the current model and those of Henriques et al. (2013) and Guo et al. (2013) are shown in Fig. S5. Note that in our new model, as in its predecessors, the mass growth of black holes through the radio mode is negligible in comparison with quasar mode accretion.

This form of growth is, however, important in that it is assumed to produce relativistic jets which deposit energy into the hot gas halo in analogy with the hot bubbles seen in galaxy clusters (McNamara & Nulsen 2007; Birzan et al.



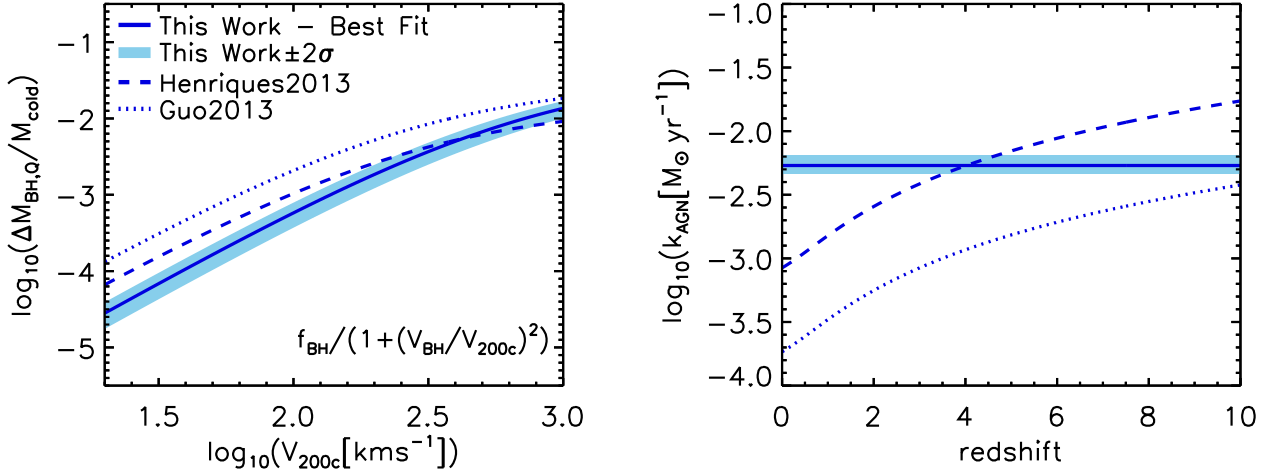


**Figure S5.** The scalings of the processes controlling black hole growth and AGN feedback. The left panel shows the maximum fraction of cold gas accreted (for a major merger of equal mass galaxies) onto central black holes during mergers (quasar accretion) as a function of virial velocity (eq. S23). The right panel shows the ratio of hot gas accretion rate to the product of hot gas and black hole masses (i.e. the coefficient in eq. S24) as a function of redshift. The additional scaling with  $V_{200c}^3/M_{200c}$  results in the redshift variation seen in models prior to this work. Accretion in this mode is assumed to suppress cooling in massive systems ( $\log M_*/M_\odot \geq 10.5$ ). In both panels the best-fitting and allowed  $\pm 2\sigma$  regions for the current model are shown as solid blue lines and light blue regions. The scalings adopted in Henriques et al. (2013) are shown as a dashed blue lines and the Guo et al. (2013) scalings as dotted blue lines.

2004). The energy input rate is taken to be

$$\dot{E}_{\text{radio}} = \eta \dot{M}_{\text{BH}} c^2, \quad (\text{S25})$$

where  $\eta = 0.1$  is an efficiency parameter and  $c$  is the speed of light. This energy then suppresses cooling from the hot gas to the cold disc, resulting in an effective cooling rate given by

$$\dot{M}_{\text{cool,eff}} = \max \left[ \dot{M}_{\text{cool}} - 2\dot{E}_{\text{radio}}/V_{200c}^2, 0 \right]. \quad (\text{S26})$$

We assume that elimination of the cooling flow also cuts off the supply of gas to the black hole, so that heating of the hot atmosphere beyond this point is not possible.

Despite growing observational and theoretical evidence for the interaction of black holes with their gaseous environment, we still lack an established theory for this process. The equations given here, like those of Croton et al. (2006), should be regarded as a purely phenomenological representation of some process which acts to prevent the cooling of gas onto massive central galaxies without requiring additional star formation. A good indication that the assumed energetic budget of the process is plausible is given in Fig. S6, where we compare our model predictions to observations of the volume-averaged AGN heating rate. The heating rate in the model is computed as  $\Omega_{\text{L mech}} = \eta \dot{M}_{\text{BH}} c^2$ , while observationally it is derived from integrating the mechanical luminosity density function. This is obtained from the AGN monochromatic radio to mechanical power (see section 7.3 of Smolčić et al. (2009)). The comparisons with observation presented in the main paper and in Paper II, in combination with Fig. S6, suggest that our current assumptions result in quenching of star formation in intermediate and high-mass galaxies approximately as required by the data.

In addition to the change of eq. S24, a feature that we recently discovered in our dark matter merger trees moti-

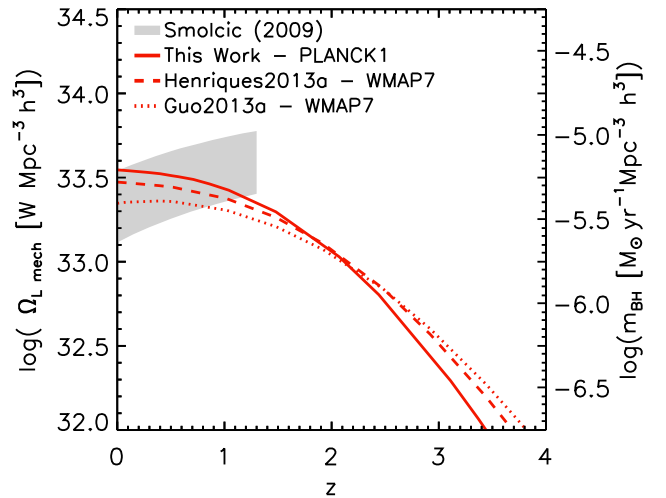


**Figure S6.** Comparison between theoretical predictions and observations for the volume-averaged AGN heating rate across cosmic time. The new model is represented by a solid red line, Henriques et al. (2013) by a dashed red line and Guo et al. (2013) by a dotted red line. Observations from the VLA-COSMOS survey (Smolčić et al. 2009) are shown as a light gray region.

vated another adjustment to our AGN radio mode feedback. For one massive dark matter structure in the Millennium Simulation, a low-mass satellite subhalo is at some point converted into the main subhalo of the FOF group. As a result, a very small galaxy with a low-mass black hole suddenly acquires  $> 10^{14} M_\odot$  of hot gas. This leads to a short episode

of catastrophic cooling that increases the stellar mass of the central galaxy by as much as two orders of magnitude.

In order to correct this numerical artefact we assume that the AGN energy left over after offsetting the cooling of hot gas in satellite galaxies can be used to offset cooling in the hot gas of their hosts (for satellites within  $R_{200}$ ). As a result, when the low-mass galaxy suddenly becomes the central object of a cluster, the energy released from black holes in other satellite galaxies is enough to suppress excessive cooling from the hot atmosphere onto the central object.

### S1.11 Environmental processes

The growth of structure in a  $\Lambda$ CDM universe affects galaxies as they and their haloes fall into larger systems and are influenced by tides, by hydrodynamical forces from the hot gas through which they move, and by encounters with other galaxies. Such environmental effects remove material and modify the structure and evolution of the galaxies, in some cases leading to their complete disruption. Several such processes are incorporated in our modelling and their treatment here follows that of Guo et al. (2011) closely. However, environmental effects appear overestimated in the earlier model, which predicts a significantly higher fraction of quenched satellite galaxies than is observed, particularly in intermediate mass haloes ( $\log M_{200}/M_{\odot} \sim 13.0$ ) (e.g. Wang et al. 2012, 2014). We address this problem here by suppressing ram-pressure stripping in such systems.

#### S1.11.1 Tidal and ram-pressure stripping

As soon a halo falls into a larger system its mass growth reverses as tidal forces begin to remove dark matter (e.g. De Lucia et al. 2004). In the Guo et al. (2011) model, this implies that no new baryonic material is added to the system and its hot gas atmosphere is stripped away in proportion to its dark matter mass,

$$\frac{M_{\text{hot}}(R_{\text{tidal}})}{M_{\text{hot, infall}}} = \frac{M_{\text{DM}}}{M_{\text{DM, infall}}}, \quad (\text{S27})$$

where the limiting radius is given by a simple ‘‘isothermal’’ model,

$$R_{\text{tidal}} = \left( \frac{M_{\text{DM}}}{M_{\text{DM, infall}}} \right) R_{\text{DM, infall}}. \quad (\text{S28})$$

In these equations,  $M_{\text{DM, infall}}$ ,  $R_{\text{DM, infall}}$  and  $M_{\text{hot, infall}}$  are  $M_{200c}$ ,  $R_{200c}$  and the hot gas mass of the halo just prior to infall, and  $M_{\text{DM}}$  and  $M_{\text{hot}}$  are the current masses of these two components. By construction, tidal stripping will have removed all hot gas once the subhalo is disrupted and the galaxy becomes an orphan.

Hot gas can also be stripped by ram-pressure effects which are followed starting when the satellite first falls within the virial radius of its host. At a certain distance  $R_{\text{r.p.}}$  from the centre of the satellite, self-gravity is approximately balanced by ram pressure:

$$\rho_{\text{sat}}(R_{\text{r.p.}}) V_{\text{sat}}^2 = \rho_{\text{par}}(R) V_{\text{orbit}}^2, \quad (\text{S29})$$

where  $\rho_{\text{sat}}(R_{\text{r.p.}})$  is the hot gas density of the satellite at radius  $R_{\text{r.p.}}$ ,  $V_{\text{sat}}$  is the virial velocity of the subhalo at infall (which we assume to be constant as the subhalo orbits around the main halo),  $\rho_{\text{par}}(R)$  is the hot gas density of the

parent dark matter halo at the distance  $R$  of the satellite from the centre of its potential well, and  $V_{\text{orbit}}$  is the orbital velocity of the satellite, which we approximate as the virial circular velocity of the main halo. The densities here are again estimated from the total mass and limiting radius of the relevant component according to an ‘‘isothermal’’ model,  $\rho \propto r^{-2}$ . Finally, the radius of the hot gas component is taken to be the smaller of  $R_{\text{r.p.}}$  and  $R_{\text{tidal}}$ .

In the current work we apply this ram-pressure model only in haloes above a threshold mass ( $M_{\text{r.p.}}$ ) which we introduce as a free parameter which observational constraints then require to be  $\sim 10^{14} M_{\odot}$ . Combined with our lower threshold for star formation, this changes reduces the excess of passive satellites found in the Guo et al. (2011) and Henriques et al. (2013) models, while remaining consistent with observation of ram-pressure stripping phenomena in rich clusters.

Finally we note that ram-pressure effects on the cold gas component are not included in our model. Such effects are expected (e.g. Bekki 2014) and are indeed observed in high density regions (e.g. Crowl et al. 2005; Fumagalli et al. 2014) but they require more extreme conditions than the effects considered in this section.

#### S1.11.2 Tidal disruption of galaxies

Our implementation of the tidal disruption of the stellar and cold gas components of galaxies is unchanged from Guo et al. (2011). Since both components are considerably more concentrated than the dark matter, we consider disruption only for galaxies that have already lost their dark matter and hot gas components. For such orphans, the baryonic (cold gas + stellar mass) density within the half-mass radius is compared to the dark matter density of the main halo within the pericentre of the satellite’s orbit. If the latter is larger, i.e.

$$\frac{M_{\text{DM, halo}}(R_{\text{peri}})}{R_{\text{peri}}^3} \equiv \rho_{\text{DM, halo}} > \rho_{\text{sat}} \equiv \frac{M_{\text{sat}}}{R_{\text{sat, half}}^3}, \quad (\text{S30})$$

the satellite is completely disrupted, its stars are added to the intracluster light (ICL) and its cold gas is added to the hot gas atmosphere of the central galaxy. The galaxy’s half-mass radius is calculated from those of the cold gas and stellar discs and the bulge (assuming exponential surface density profiles for the first two and a surface density scaling with  $r^{1/4}$  for the latter), while its orbital pericentre is calculated as

$$\left( \frac{R}{R_{\text{peri}}} \right)^2 = \frac{\ln R/R_{\text{peri}} + \frac{1}{2}(V/V_{200c})^2}{\frac{1}{2}(V_t/V_{200c})^2}, \quad (\text{S31})$$

assuming conservation of energy and angular momentum and a singular isothermal potential for the orbit,  $\phi(R) = V_{200c}^2 \ln R$ . In these equations,  $R$  is the current distance of the satellite from halo centre, and  $V$  and  $V_t$  are the total and tangential velocities of the satellite with respect to halo centre (see Section S1.12.1 for a description on how these are determined for orphans). We tested that this condition for complete disruption of satellites gives very similar answers to the more detailed implementation of gradual stripping proposed by Henriques & Thomas (2010) (See Contini et al. (2014) for a more extensive comparison of different implementations of tidal disruption).

### S1.11.3 SN feedback in orphan galaxies

For orphan galaxies environmental effects are particularly dramatic. Since our implementation of tidal stripping of hot gas is directly connected to the stripping of dark matter, once galaxies lose their halo, they also have no hot gas left. As described in Section S1.7.1, from this point on, we also assume that any cold gas reheated by star formation activity leaves the galaxy and is added to the hot gas atmosphere of the main halo. This can lead to rapid depletion of any remaining cold gas.

## S1.12 Mergers and bulge formation

### S1.12.1 Positions and velocities of orphans

Once a satellite subhalo is disrupted, its central galaxy becomes an orphan and its position and velocity are linked to those of the dark matter particle which was most strongly bound within the subhalo just prior to its disruption. As soon as a disruption event occurs, this particle is identified and a merging clock is started, based on an estimate of how long the satellite will take to spiral into the central object due to dynamical friction. This time is computed using the Binney & Tremaine (1987) formula:

$$t_{\text{friction}} = \alpha_{\text{friction}} \frac{V_{200c}^2 r_{\text{sat}}^2}{GM_{\text{sat}} \ln \Lambda}, \quad (\text{S32})$$

where  $M_{\text{sat}}$  is the total mass of the satellite (dark and baryonic),  $\ln \Lambda = \ln(1 + M_{200c}/M_{\text{sat}})$  is the Coulomb logarithm and  $\alpha_{\text{friction}} = 2.4$  is a parameter originally set by De Lucia & Blaizot (2007) to match the bright end of the  $z = 0$  luminosity functions. This value was later shown to be consistent with inferences from direct numerical simulation (Boylan-Kolchin et al. 2008; De Lucia et al. 2010) but should still be considered poorly known. The Millennium-II simulation is able to resolve subhaloes which have been stripped to masses below that of their central galaxy. In such cases we turn on the merging clock as soon as the subhalo mass drops below the stellar mass in the galaxy.

Following Guo et al. (2011) we model the decay of the satellite’s orbit due to dynamical friction by placing the orphan galaxy not at the current position of the particle with which it is identified, but at a position whose (vector) offset from the central galaxy is reduced from that of the particle by a factor of  $(1 - \Delta t/t_{\text{friction}})$  where  $\Delta t$  is the time since the dynamical friction clock was started. The (vector) velocity of the orphan galaxy is set equal to that of the tagged particle. This time dependence is based on a simple model for a satellite with “isothermal” density structure spiralling to the centre of an isothermal host on a circular orbit. When  $\Delta t = t_{\text{friction}}$  the orphan merges with the central galaxy.

### S1.12.2 Merger-triggered star formation

When a satellite finally merges with the object at the centre of the main halo, the outcome is different for major and minor mergers. We define a major merger to be one in which the total baryonic mass of the less massive galaxy exceeds a fraction  $R_{\text{merge}}$  of that of the more massive galaxy. In a major merger, the discs of the two progenitors are destroyed and all their stars become part of the bulge of the descendent, along with any stars formed during the merger. In a

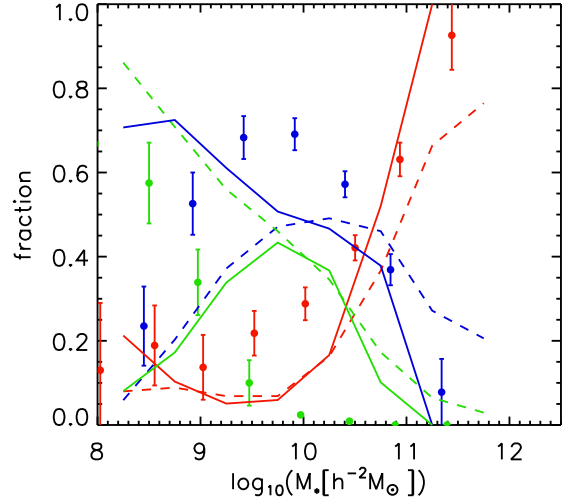


**Figure S7.** Comparison between theoretical predictions and observations for the fraction of different morphological types as a function of stellar mass. Red lines show the fraction of ellipticals ( $M_{\text{bulge}}/M_{\text{total}} > 0.7$ ), blue lines show the fraction of normal spirals ( $0.01 < M_{\text{bulge}}/M_{\text{total}} < 0.7$ ) and green lines represent pure discs or extreme late-types ( $M_{\text{bulge}}/M_{\text{total}} < 0.01$ ). Solid and dashed lines indicate predictions based on the MII and MR simulations, respectively. Observational data points from Conzelmann (2006) are represented by the filled circles.

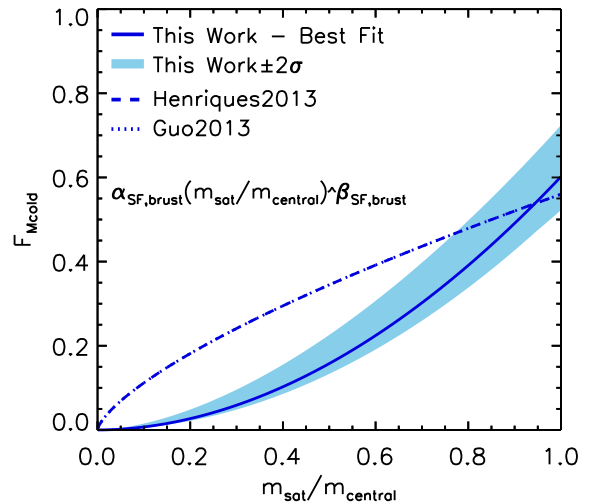


**Figure S8.** The fraction of cold gas converted to stars in merger-triggered starbursts as a function of the mass ratio between satellite and central galaxies. The best-fitting and  $\pm 2\sigma$  regions for the current model are shown as a solid blue line and a light blue region respectively. The scaling adopted in Henriques et al. (2013) and Guo et al. (2013) is shown as a dashed blue line.

minor merger, the disc of the larger progenitor survives and accretes the cold gas component of the smaller galaxy, while its bulge accretes all the stars of the victim. Stars formed during the merger stay in the disc of the descendent. In both types of merger, cold gas is fed to the central black hole according to the formulae of Section S1.10.1.  $R_{\text{merge}}$  is fixed and not included in the MCMC analysis since we find some tension between the values required for model predictions to reproduce observed colours and observed morphologies. Our adopted value of 0.1, slightly compromises the agreement with the observed red fraction of galaxies at  $z = 1$ , but ensures that the morphologies of massive galaxies in the model are reasonably close to observations. This comparison is shown in Fig. S7. Some discrepancies remain at low mass, particularly for MR11, where there is an excess of normal spirals with respect to pure disc galaxies.

The stellar mass formed during a merger is modelled using the ‘‘collisional starburst’’ formulation of Somerville et al. (2001):

$$M_{\star, \text{burst}} = \alpha_{\text{SF, burst}} \left( \frac{M_1}{M_2} \right)^{\beta_{\text{SF, burst}}} M_{\text{cold}}, \quad (\text{S33})$$

where  $M_1 < M_2$  are the baryonic masses of the two galaxies, and  $M_{\text{cold}}$  is their total cold gas mass. The  $\alpha_{\text{SF, burst}}$  and  $\beta_{\text{SF, burst}}$  parameters were originally fixed to reflect the results of the Mihos & Hernquist (1996) simulations, but in the current work they are left free and are allowed to vary in our MCMC analysis. Despite this, in our best-fitting model the fraction of cold gas converted to stars in merger-related bursts is relatively close to what was previously assumed. Fig. S8 compares this quantity for our current model (solid blue line and light blue regions) to that assumed in the models of Henriques et al. (2013) and Guo et al. (2013) (dashed blue line).

### S1.12.3 Bulge Formation

In our model bulges can form through major and minor mergers and through the buckling instability of discs. After a major merger, all stars are considered part of the new bulge, but the remnant of a minor merger retains the stellar disc of the larger progenitor and its bulge gains only the stars from the smaller progenitor. Following Guo et al. (2011), we use energy conservation and the virial theorem to compute the change in sizes in both minor and major mergers:

$$\frac{GM_{\text{new, bulge}}^2}{R_{\text{new, bulge}}} = \frac{GM_1^2}{R_1} + \frac{GM_2^2}{R_2} + 2\alpha_{\text{inter}} \frac{GM_1 M_2}{R_1 + R_2}, \quad (\text{S34})$$

where the left-hand side represents the binding energy of the final bulge, the first two terms of the right-hand side represent the binding energies of the progenitor stellar systems (the radii in these three terms are taken to be the half-mass radii of the corresponding stellar systems) and the last term is the binding energy of the relative orbit of the two progenitors at the time of merger. The coefficient  $\alpha_{\text{inter}}$  quantifies the binding energy invested in this orbit relative to that in the individual systems. Guo et al. (2011) set  $\alpha_{\text{inter}} = 0.5$  and show that this leads to bulge sizes in reasonable agreement with SDSS data. When either of the progenitors is a composite disc+bulge system, its half-mass radius is calculated assuming an exponential disc and an  $r^{1/4}$ -law bulge.

Another important channel of bulge growth is secular evolution through disc instabilities. These dynamical instabilities occur through the formation of bars which then buckle. They transport material inwards to the bulge and they occur in galaxies where self-gravity of the disc dominates the gravitational effects of the bulge and halo. As a criterion for disc instability, we follow Guo et al. (2011) in adopting

$$V_{\text{max}} < \sqrt{\frac{GM_{\star, d}}{3R_{\star, d}}}, \quad (\text{S35})$$

where  $M_{\star, d}$  and  $R_{\star, d}$  are the stellar mass and exponential scale-length of the stellar disc and  $V_{\text{max}}$  is the maximum circular velocity of the host dark matter halo hosting the disc.

When the instability criterion of eq. S35 is met, we transfer sufficient stellar mass from the disc to the bulge to make the disc marginally stable again. Following Guo et al. (2011) we assume that this mass  $\delta M_{\star}$  is transferred from the innermost part of the disc. Thus, the half-mass radius of the material to be added to the bulge,  $R_b$ , is related to  $\delta M_{\star}$  through

$$\delta M_{\star} = 2\pi \Sigma_{\star 0} R_{\star, d} [R_{\star, d} - (R_b + R_{\star, d}) \exp(-R_b/R_{\star, d})], \quad (\text{S36})$$

where  $\Sigma_{\star 0}$  and  $R_{\star, d}$  are the central surface density and exponential scale-length of the unstable disc. We neglect the angular momentum of the transferred material, so the disc’s angular momentum is unchanged, resulting in an increase in  $R_{\star, d}$  to compensate for the mass lost.

If the galaxy already has a spheroidal component, the newly created bulge material is assumed to merge with the existing bulge according to eq. (S34) where we now take  $\alpha_{\text{inter}} = 2$  to account for the fact that the inner disc and the initial bulge are concentric and have no relative motion. For further discussion of this model for bulge growth and for comparisons with observational data we refer the reader to Guo et al. (2011).

### S1.13 Stellar populations synthesis

Stellar population synthesis models are a crucial part of galaxy formation theory as they link the masses, ages and metallicities predicted for stars to the observable emission at various wavelengths. We use Maraston (2005) as our default stellar population synthesis model, but we have checked that the publicly released but still unpublished Charlot & Bruzual (2007) code leads to very similar results for all the properties we consider. Somewhat different predictions are obtained with the earlier Bruzual & Charlot (2003) code because of the weaker emission it assumes for the TP-AGB stage of evolution of intermediate age stars. Recent work by a number of authors suggests that the more recent models are in better agreement with observed near-infrared emission from bright galaxies at  $z \geq 2$  (Henriques et al. 2011, 2012; Tonini et al. 2009, 2010; Fontanot & Monaco 2010; Tonini et al. 2011; Gonzalez-Perez et al. 2014). For the Munich galaxy formation model, in particular, Henriques et al. (2011) and Henriques et al. (2012) showed that Maraston (2005) or Charlot & Bruzual (2007) populations give stellar mass and  $K$ -band luminosity functions for which the massive/bright end agrees with observation from  $z = 3$  to 0.

Nevertheless, as part of our model release we will, for comparison purposes, also include luminosities computed using Bruzual & Charlot (2003) stellar populations.

### S1.14 Dust Model

Actively star-forming galaxies are known to be rich in dust. This can have a dramatic effect on their emitted spectrum since dust significantly absorbs optical/UV light while having a much milder effect at longer wavelengths. As a result, dust-dominated galaxies will generally have red colours even if they are strongly star forming. We follow De Lucia & Blaizot (2007) in considering dust extinction separately for the diffuse interstellar medium (ISM) (following Devriendt et al. 1999) and for the molecular birth clouds within which stars form (following Charlot & Fall 2000)). The optical depth of dust as a function of wavelength is computed separately for each component and then a slab geometry is assumed in order to compute the total extinction of the relevant populations. We do not at present attempt to compute the detailed properties of the dust particles or the re-emission of the absorbed light.

#### S1.14.1 Extinction by the ISM

The optical depth of diffuse dust in galactic discs is assumed to vary with wavelength as

$$\tau_{\lambda}^{ISM} = (1+z)^{-1} \left( \frac{A_{\lambda}}{A_V} \right)_{Z_{\odot}} \left( \frac{Z_{\text{gas}}}{Z_{\odot}} \right)^s \times \left( \frac{\langle N_H \rangle}{2.1 \times 10^{21} \text{ atoms cm}^{-2}} \right), \quad (\text{S37})$$

where  $\langle N_H \rangle$  represents the mean column density of hydrogen and is given by

$$\langle N_H \rangle = \frac{M_{\text{cold}}}{1.4 m_p \pi (a R_{\text{gas,d}})^2}. \quad (\text{S38})$$

Here  $R_{\text{gas,d}}$  is the cold gas disc scale-length, 1.4 accounts for the presence of helium and  $a = 1.68$  in order for  $\langle N_H \rangle$  to represent the mass-weighted average column density of an exponential disc. Following the results in Guiderdoni & Rocca-Volmerange (1987), the extinction curve in eq. (S37) depends on the gas metallicity and is based on an interpolation between the Solar Neighbourhood and the Large and Small Magellanic Clouds:  $s = 1.35$  for  $\lambda < 2000 \text{ \AA}$  and  $s = 1.6$  for  $\lambda > 2000 \text{ \AA}$ . The extinction curve for solar metallicity,  $(A_{\lambda}/A_V)_{Z_{\odot}}$ , is taken from Mathis et al. (1983).

The redshift dependence in eq. (S37) is significantly stronger than in previous versions of our model ( $(1+z)^{-0.5}$  in Kitzbichler & White (2007) and  $(1+z)^{-0.4}$  in Guo & White (2009). The dependence implies that for the same amount of cold gas and the same metal abundance, there is less dust at high redshift. The motivation comes both from observations (Steidel et al. 2004; Quadri et al. 2008) and from the assumption that dust is produced by relatively long-lived stars. However, it may also be that this redshift dependence has to be introduced as a phenomenological compensation for the excessively early build-up of the metal content in model galaxies shown in Fig. S3. In practice we include it merely as representation of the observed

extinction behaviour (Bouwens et al. 2014), while the physical reason for discrepancy with the simple model remains to be established. As will be shown in Clay et al. (2015) this produces luminosity functions and extinction estimates for Lyman-break galaxies at  $z > 5$  compatible with HST data.

#### S1.14.2 Extinction by molecular clouds

This second source of extinction affects only young stars. Following Charlot & Fall (2000), our model assumes that such extinction affects stars younger than the lifetime of stellar birth clouds (taken to be  $10^7$  years). The relevant optical depth is taken to be

$$\tau_{\lambda}^{BC} = \tau_{\lambda}^{ISM} \left( \frac{1}{\mu} - 1 \right) \left( \frac{\lambda}{5500 \text{ \AA}} \right)^{-0.7}, \quad (\text{S39})$$

where  $\mu$  is given by a random Gaussian deviate with mean 0.3 and standard deviation 0.2, truncated at 0.1 and 1.

#### S1.14.3 Overall extinction curve

In order to get the final overall extinction, every galaxy is assigned an inclination given by the angle between the disc angular momentum and the  $z$ -direction of the simulation box, and a ‘‘slab’’ geometry is assumed for the dust in the diffuse ISM. For sources that are uniformly distributed within the disc then the mean absorption coefficient is

$$A_{\lambda}^{ISM} = -2.5 \log_{10} \left( \frac{1 - \exp^{-\tau_{\lambda}^{ISM} \sec \theta}}{\tau_{\lambda}^{ISM} \sec \theta} \right), \quad (\text{S40})$$

where  $\theta$  is the angle of inclination of the galaxy relative to the line-of-sight. Emission from young stars embedded within birth clouds is subject to an additional extinction of

$$A_{\lambda}^{BC} = -2.5 \log_{10} \left( \exp^{-\tau_{\lambda}^{BC}} \right). \quad (\text{S41})$$

### S1.15 Monte Carlo Markov Chains

In order to sample the full multidimensional parameter space of our model we use MCMC techniques. This enables exploration of the allowed regions when the model is constrained by a broad variety of calibrating observations, which may be of different types and correspond to different redshifts. The same scheme allows us to assess the merits of different implementations of critical astrophysical processes. We use a version of the Metropolis-Hastings method (Metropolis et al. 1953; Hastings 1970); a full description of the algorithm can be found in Section 3 of Henriques et al. (2009). A full MCMC chain requires evaluation of many tens of thousands of models and it is not computationally feasible to build all of these models for the full Millennium or Millennium-II simulation. We therefore use sampling techniques to construct a representative subset of subhalo merger trees on which the galaxy formation model is evaluated during the MCMC procedure (details are given in Appendix 2 of Henriques et al. 2013). Once the best-fitting model has been identified, it can be implemented on the full volumes of the two simulations.

Fig. S9 shows marginalized 1D posterior distributions for our model parameters when the model is constrained by observational data on the abundance and passive fraction of galaxies as a function of stellar mass from  $z = 3$  down to

**Table S1.** Results from the MCMC parameter estimation. The best-fitting values of parameters and their “2- $\sigma$ ” confidence limits are compared with the values published in Henriques et al. (2013) and Guo et al. (2013).

	Guo13	Henriques13	New Best Fit	2 $\sigma$ lower	2 $\sigma$ upper	Units
$\alpha_{\text{SF}}$ (SF eff - eq. S14)	0.011	0.055	0.025	0.021	0.029	
$M_{\text{crit},0}$ (Gas mass threshold - eq. S15)	0.38	0.38	0.24	0.20	0.27	$10^{10} M_{\odot}$
$\alpha_{\text{SF,burst}}$ (SF burst eff - eq. S33)	0.56	0.56	0.60	0.52	0.73	
$\beta_{\text{SF,burst}}$ (SF burst slope - eq. S33)	0.70	0.70	1.9	1.7	2.0	
$k_{\text{AGN}}$ (Radio feedback eff - eq. S24)	new eq	new eq	$5.3 \times 10^{-3}$	$4.6 \times 10^{-3}$	$6.5 \times 10^{-3}$	$M_{\odot} \text{ yr}^{-1}$
$f_{\text{BH}}$ (BH growth eff - eq. S23)	0.03	0.015	0.041	0.035	0.048	
$V_{\text{BH}}$ (Quasar growth scale - eq. S23)	280	280	750	670	880	$\text{km s}^{-1}$
$\epsilon$ (Mass-loading eff - eq. S19)	4.0	2.1	2.6	1.9	2.6	
$V_{\text{reheat}}$ (Mass-loading scale - eq. S19)	80	405	480	390	540	$\text{km s}^{-1}$
$\beta_1$ (Mass-loading slope - eq. S19)	3.2	0.92	0.72	0.60	0.82	
$\eta$ (SN ejection eff - eq. S17)	0.18	0.65	0.62	0.53	0.68	
$V_{\text{eject}}$ (SN ejection scale - eq. S17)	90	336	100	90	120	$\text{km s}^{-1}$
$\beta_2$ (SN ejection slope - eq. S17)	3.2	0.46	0.80	0.71	0.95	
$\gamma$ (Ejecta reincorporation - eq. S22)	new eq	$1.8 \times 10^{10}$	$3.0 \times 10^{10}$	$2.6 \times 10^{10}$	$3.6 \times 10^{10}$	yr
$M_{\text{r.p.}}$ (Ram-pressure threshold)	0.0	0.0	$1.2 \times 10^4$	$1.1 \times 10^4$	$1.6 \times 10^4$	$10^{10} M_{\odot}$
$R_{\text{merger}}$ (Major-merger threshold)	0.30	0.30	0.1			
$\alpha_{\text{friction}}$ (Dynamical friction - eq. S32)	2.0	2.0	2.5	2.1	2.8	
$y$ (Metal yield)	0.03	0.047	0.046	0.038	0.053	

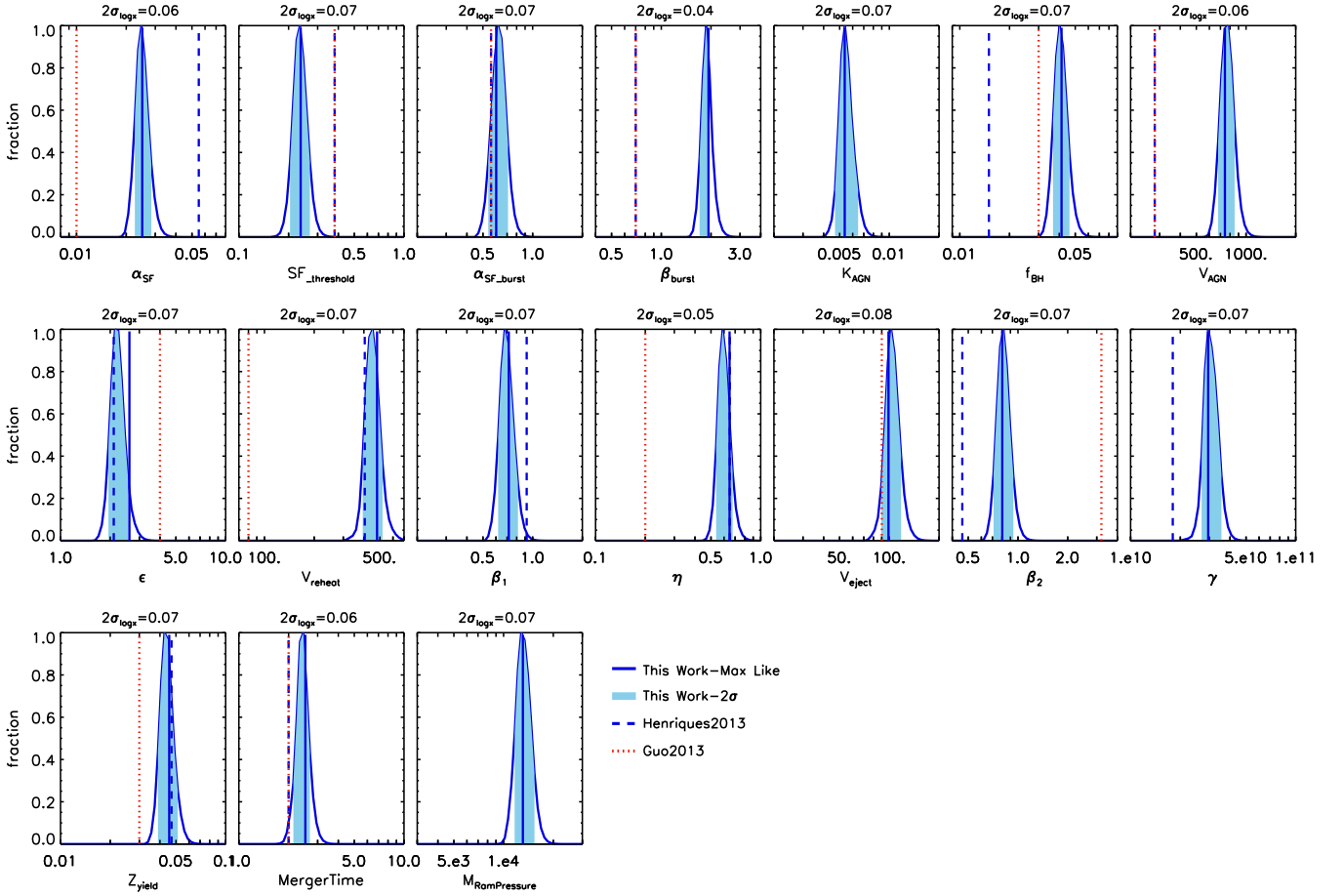
$z = 0$ . Vertical solid blue lines correspond to the parameter values of the best-fitting model (taken to be the one for which the MCMC chain found the highest likelihood) and these are also presented in Table S1. Shaded blue regions show the central 95% confidence region of each marginalized posterior distribution and the boundaries of the corresponding parameter interval are also given in Table S1. Interestingly, although the best-fitting model has parameters which lie within these regions in almost all cases, this is not true for  $k_{\text{AGN}}$  and  $V_{\text{reheat}}$ . The allowed parameter range is quite narrow in all cases, showing that these observations are sufficient to specify our model completely without major degeneracies.

Fig. S9 also shows the parameter values corresponding to the best-fitting models of Henriques et al. (2013) (dashed vertical blue lines) and Guo et al. (2013) (dotted vertical blue lines). Despite changes in cosmology and in several aspects of the astrophysical modelling, the efficiencies of most processes are very similar in the different versions of the model (see also Figs S2, S5 and S8). This indicates that parameters which were not previously included in the MCMC sampling (all of them in the case of Guo et al. (2013)!) were, in fact, well constrained by less rigorous comparison to observations. The exceptions are the cold gas density threshold for star formation, which now has a significantly lower value, and the ram-pressure stripping threshold, which was zero in the earlier models. Both changes are required to predict the correct evolution of the fraction of passive galaxies as a function of stellar mass, which simply could not be explained by the previous models. Indeed, if we were to carry out an MCMC analysis of the Henriques et al. (2013) or the Guo et al. (2013) model using this observational constraint, we would find a very low maximum likelihood value. As a result, we do not need to integrate over the posterior distributions to perform Bayesian model selection – the current

model is the only one of the three which can come close to representing the observational distributions used as constraints.

## REFERENCES

- Angulo R. E., Hilbert S., 2015, *MNRAS*, 448, 364  
 Angulo R. E., White S. D. M., 2010, *MNRAS*, 405, 143  
 Bekki K., 2014, *MNRAS*, 438, 444  
 Benson A. J., Pearce F. R., Frenk C. S., Baugh C. M., Jenkins A., 2001, *MNRAS*, 320, 261  
 Bertone S., De Lucia G., Thomas P. A., 2007, *MNRAS*, 379, 1143  
 Bigiel F., Leroy A., Walter F., Brinks E., de Blok W. J. G., Madore B., Thornley M. D., 2008, *AJ*, 136, 2846  
 Binney J., Tremaine S., 1987, *Galactic dynamics*. Princeton, NJ, Princeton University Press, 1987, 747 p.  
 Birnboim Y., Dekel A., 2003, *MNRAS*, 345, 349  
 Bîrzan L., Rafferty D. A., McNamara B. R., Wise M. W., Nulsen P. E. J., 2004, *ApJ*, 607, 800  
 Bothwell M. S., et al., 2014, *MNRAS*, 445, 2599  
 Bouwens R. J., et al., 2014, *ApJ*, 793, 115  
 Boylan-Kolchin M., Ma C.-P., Quataert E., 2008, *MNRAS*, 383, 93  
 Boylan-Kolchin M., Springel V., White S. D. M., Jenkins A., Lemson G., 2009, *MNRAS*, 398, 1150  
 Bruzual G., Charlot S., 2003, *MNRAS*, 344, 1000  
 Chabrier G., 2003, *PASP*, 115, 763  
 Charlot S., Bruzual G., 2007, provided to the community but not published  
 Charlot S., Fall S. M., 2000, *ApJ*, 539, 718  
 Clay S. J., Thomas P. A., Henriques B. M. B., Wilkins S. M., 2015, *MNRAS*, in press  
 Colless M., et al., 2001, *MNRAS*, 328, 1039



**Figure S9.** Shaded blue regions show the 1D, normalised posterior distributions of our model parameters when the model is constrained by observations of the abundance and passive fraction of galaxies as a function of stellar mass from  $z = 3$  to 0. Straight lines represent values corresponding to our overall best-fitting model (solid blue lines) and to those of Henriques et al. (2013) (dashed blue lines) and Guo et al. (2013) (dotted red lines). The  $x$ -axis is plotted logarithmically in all cases.

- Conselice C. J., 2006, MNRAS, 373, 1389  
 Contini E., De Lucia G., Villalobos Á., Borgani S., 2014, MNRAS, 437, 3787  
 Croton D. J., et al., 2006, MNRAS, 365, 11  
 Crowl H. H., Kenney J. D. P., van Gorkom J. H., Vollmer B., 2005, AJ, 130, 65  
 Davis M., Efstathiou G., Frenk C. S., White S. D. M., 1985, ApJ, 292, 371  
 De Lucia G., Blaizot J., 2007, MNRAS, 375, 2  
 De Lucia G., Boylan-Kolchin M., Benson A. J., Fontanot F., Monaco P., 2010, MNRAS, 406, 1533  
 De Lucia G., Kauffmann G., Springel V., White S. D. M., Lanzoni B., Stoehr F., Tormen G., Yoshida N., 2004, MNRAS, 348, 333  
 De Lucia G., Kauffmann G., White S. D. M., 2004, MNRAS, 349, 1101  
 De Lucia G., Tornatore L., Frenk C. S., Helmi A., Navarro J. F., White S. D. M., 2014, ArXiv e-prints  
 Dekel A., Silk J., 1986, ApJ, 303, 39  
 Devriendt J. E. G., Guiderdoni B., Sadat R., 1999, Astronomy and Astrophysics Supplement Series, 350, 381  
 Efstathiou G., 1992, MNRAS, 256, 43P  
 Fontanot F., Monaco P., 2010, MNRAS, 405, 705  
 Fontanot F., Somerville R. S., Silva L., Monaco P., Skibba R., 2009, MNRAS, 392, 553  
 Forcada-Miro M. I., White S. D. M., 1997, preprint (arXiv:astro-ph/9712204)  
 Fu J., Kauffmann G., Huang M.-l., Yates R. M., Moran S., Heckman T. M., Davé R., Guo Q., Henriques B. M. B., 2013, MNRAS, 434, 1531  
 Fu J., Kauffmann G., Li C., Guo Q., 2012, MNRAS, 424, 2701  
 Fumagalli M., Fossati M., Hau G. K. T., Gavazzi G., Bower R., Sun M., Boselli A., 2014, ArXiv e-prints, 1407.7527  
 Gallazzi A., Charlot S., Brinchmann J., White S. D. M., Tremonti C. A., 2005, MNRAS, 362, 41  
 Genel S., et al., 2014, preprint (arXiv:1405.3749)  
 Gnedin N. Y., 2000, ApJ, 542, 535  
 Gonzalez-Perez V., Lacey C. G., Baugh C. M., Lagos C. D. P., Helly J., Campbell D. J. R., Mitchell P. D., 2014, MNRAS  
 Guiderdoni B., Rocca-Volmerange B., 1987, Astronomy and Astrophysics Supplement Series, 186, 1  
 Guo Q., White S., Angulo R. E., Henriques B., Lemson G., Boylan-Kolchin M., Thomas P., Short C., 2013, MNRAS, p. 135  
 Guo Q., White S., Boylan-Kolchin M., De Lucia G., Kauffmann G., Lemson G., Li C., Springel V., Weinmann S.,

- 2011, MNRAS, 413, 101
- Guo Q., White S. D. M., 2009, MNRAS, 396, 39
- Hastings W. K., 1970, Biometrika, 57, 97
- Haynes M. P., et al., 2011, AJ, 142, 170
- Heiderman A., Evans II N. J., Allen L. E., Huard T., Heyer M., 2010, ApJ, 723, 1019
- Henriques B., Maraston C., Monaco P., Fontanot F., Menci N., De Lucia G., Tonini C., 2011, MNRAS, 415, 3571
- Henriques B. M. B., Thomas P. A., 2010, MNRAS, 403, 768
- Henriques B. M. B., Thomas P. A., Oliver S., Roseboom I., 2009, MNRAS, 396, 535
- Henriques B. M. B., White S. D. M., Lemson G., Thomas P. A., Guo Q., Marleau G.-D., Overzier R. A., 2012, MNRAS, 421, 2904
- Henriques B. M. B., White S. D. M., Thomas P. A., Angulo R. E., Guo Q., Lemson G., Springel V., 2013, MNRAS, 431, 3373
- Kauffmann G., 1996, MNRAS, 281, 487
- Kauffmann G., Colberg J., Diaferio A., White S., 1999, MNRAS, 303, 188
- Kauffmann G., White S. D. M., Guiderdoni B., 1993, MNRAS, 264, 201
- Kereš D., Katz N., Weinberg D. H., Davé R., 2005, MNRAS, 363, 2
- Kitzbichler M. G., White S. D. M., 2007, MNRAS, 376, 2
- Lada C. J., Lombardi M., Alves J. F., 2010, ApJ, 724, 687
- Lagos C. D. P., Baugh C. M., Lacey C. G., Benson A. J., Kim H.-S., Power C., 2011, MNRAS, 418, 1649
- Larson R. B., 1974, MNRAS, 169, 229
- Leroy A. K., Walter F., Brinks E., Bigiel F., de Blok W. J. G., Madore B., Thornley M. D., 2008, AJ, 136, 2782
- Lu Y., et al., 2014, ApJ, 795, 123
- Maiolino R., et al., 2008, Astronomy and Astrophysics Supplement Series, 488, 463
- Maraston C., 2005, MNRAS, 362, 799
- Martin C. L., Shapley A. E., Coil A. L., Kornei K. A., Bundy K., Weiner B. J., Noeske K. G., Schiminovich D., 2012, ApJ, 760, 127
- Mathis J. S., Mezger P. G., Panagia N., 1983, Astronomy and Astrophysics Supplement Series, 128, 212
- McConnell N. J., Ma C.-P., 2013, ApJ, 764, 184
- McNamara B. R., Nulsen P. E. J., 2007, ARA&A, 45, 117
- Metropolis N., Rosenbluth A., Rosenbluth M., Teller A., Teller E., 1953, J. Chem. Phys., 21, 1087
- Mihos J. C., Hernquist L., 1996, ApJ, 464, 641
- Nelson D., Vogelsberger M., Genel S., Sijacki D., Kereš D., Springel V., Hernquist L., 2013, MNRAS, 429, 3353
- Okamoto T., Gao L., Theuns T., 2008, MNRAS, 390, 920
- Oppenheimer B. D., Davé R., 2008, MNRAS, 387, 577
- Oppenheimer B. D., Davé R., Kereš D., Fardal M., Katz N., Kollmeier J. A., Weinberg D. H., 2010, MNRAS, 406, 2325
- Quadri R. F., Williams R. J., Lee K.-S., Franx M., van Dokkum P., Brammer G. B., 2008, ApJ, 685, L1
- Rubin K. H. R., Prochaska J. X., Koo D. C., Phillips A. C., Martin C. L., Winstrom L. O., 2013, preprint (ArXiv:1307.1476)
- Rupke D. S., Veilleux S., Sanders D. B., 2005, ApJS, 160, 115
- Saintonge A., et al., 2011, MNRAS, 415, 32
- Shapley A. E., Steidel C. C., Pettini M., Adelberger K. L., 2003, ApJ, 588, 65
- Smolčić V., et al., 2009, ApJ, 696, 24
- Somerville R. S., Primack J. R., Faber S. M., 2001, MNRAS, 320, 504
- Spergel D. N., et al., 2003, ApJS, 148, 175
- Springel V., et al., 2005, Nature, 435, 629
- Springel V., White S. D. M., Tormen G., Kauffmann G., 2001, MNRAS, 328, 726
- Steidel C. C., Shapley A. E., Pettini M., Adelberger K. L., Erb D. K., Reddy N. A., Hunt M. P., 2004, ApJ, 604, 534
- Sutherland R. S., Dopita M. A., 1993, ApJS, 88, 253
- Tonini C., Maraston C., Devriendt J., Thomas D., Silk J., 2009, MNRAS, 396, L36
- Tonini C., Maraston C., Thomas D., Devriendt J., Silk J., 2010, MNRAS, 403, 1749
- Tonini C., Maraston C., Ziegler B., Böhm A., Thomas D., Devriendt J., Silk J., 2011, MNRAS, 415, 811
- Vogelsberger M., et al., 2014, Nature, 509, 177
- Wang L., Weinmann S. M., Neistein E., 2012, MNRAS, 421, 3450
- Wang W., Sales L. V., Henriques B. M. B., White S. D. M., 2014, MNRAS, 442, 1363
- Weiner B. J., Coil A. L., Prochaska J. X., Newman J. A., Cooper M. C., Bundy K., Conselice C. J., Dutton A. A., Faber S. M., Koo D. C., Lotz J. M., Rieke G. H., Rubin K. H. R., 2009, ApJ, 692, 187
- Weinmann S. M., Pasquali A., Oppenheimer B. D., Finlator K., Mendel J. T., Crain R. A., Macciò A. V., 2012, MNRAS, 426, 2797
- White S. D. M., 1989, in Frenk C. S., Ellis R. S., Shanks T., Heavens A. R., Peacock J. A., eds, Proc. NATO ASIC Vol. 264, The Epoch of Galaxy Formation Observable signatures of young galaxies. p. 15
- White S. D. M., Frenk C. S., 1991, ApJ, 379, 52
- White S. D. M., Rees M. J., 1978, MNRAS, 183, 341
- Yates R. M., Henriques B., Thomas P. A., Kauffmann G., Johansson J., White S. D. M., 2013, MNRAS, 435, 3500
- Yoshida N., Stoehr F., Springel V., White S. D. M., 2002, MNRAS, 335, 762
- Zwaan M. A., Meyer M. J., Staveley-Smith L., Webster R. L., 2005, MNRAS, 359, L30